Protein disorder-order interplay to guide the growth of hierarchical mineralized structures

Sherif Elsharkawy[1,2,3], Maisoon Al-Jawad[3,4], Maria F. Pantano[5], Esther Tejeda-Montes[2], Khushbu Mehta[2], Hasan Jamal[2], Shweta Agarwal[6,7], Kseniya Shuturminska[1,3], Alistair Rice[6], Nadezda V. Tarakina[2], Rory M. Wilson[2,4], Andy J. Bushby[2,4], Matilde Alonso[8], Jose C. Rodriguez-Cabello[8], Ettore Barbieri[2,9], Armando del Rio Hernández[6], Molly M. Stevens[6,7,10], Nicola M. Pugno[5,2,11], Paul Anderson[1,3], Alvaro Mata[1,2*]

[1]Institute of Bioengineering, Queen Mary University of London, London E1 4NS, United Kingdom. [2]School of Engineering and Materials Science, Queen Mary University of London, London E1 4NS, United Kingdom. [3]Institute of Dentistry, Barts and The London School of Medicine and Dentistry, Queen Mary University of London, London E1 4NS, United Kingdom. [4]Materials Research Institute, Queen Mary University of London, London E1 4NS, United Kingdom. [5]Laboratory of Bio-Inspired and Graphene Nanomechanics, Department of Civil, Environmental and Mechanical Engineering, University of Trento, 38123 Trento, Italy. [6]Department of Materials, Imperial College London, London SW7 2AZ, United Kingdom. [7]Department of Bioengineering, Imperial College London, London SW7 2AZ, United Kingdom. [8]G.I.R. Bioforge, University of Valladolid, CIBER-BBN, Valladolid, 47011, Spain. [9]Department of Mathematical Science and Advanced Technology, Japan Agency for Marine-Earth Science and Technology, Yokohama Institute for Earth Sciences 3173-25, Showa-machi, Kanazawa-ku, Yokohama-city, Kanagawa, 236-0001, Japan. [10]Institute of Biomedical Engineering, Imperial College London, London SW7 2AZ, United Kingdom. [11]Ket-Lab, Edoardo Amaldi Foundation, Italian Space Agency, Via del Politecnico snc, 00133 Rome, Italy *e-mail: a.mata@qmul.ac.uk

Abstract

A major goal in materials science is to develop bioinspired functional materials based on the precise control of molecular building-blocks across length-scales. Here we report a protein-mediated mineralization process that takes advantage of disorder-order interplay using elastin-like recombinamers to program organic-inorganic interactions into hierarchically-ordered mineralized structures. The materials comprise elongated apatite nanocrystals that are aligned and organized into microscopic prisms, which grow together into spherulite-like structures hundreds of microns in diameter that come together to fill macroscopic areas. The structures can be grown over large uneven surfaces and native tissues as acid resistant membranes or coatings with tuneable hierarchy, stiffness, and hardness. Our study represents a potential strategy for complex materials design that may open opportunities for hard tissue repair and provide insights into the role of molecular disorder in human physiology and pathology.

Nature is rich with examples of sophisticated materials displaying outstanding properties that emerge from their specific hierarchical structure[1]. Materials such as nacre, bone, and dental enamel possess distinct structural organization at different length-scales, which enhance their bulk material properties and functionality[2]. The capacity to create synthetic materials that emulate such ingenious architectures represents a major goal in materials science and an opportunity to tune and profoundly improve functionality[3]. In particular, the field of biomaterials would greatly benefit from the functionalities that can emerge from well-defined hierarchical organizations[4].

Biomineralization, the process by which minerals are formed by living organisms under strict biological control, is responsible for the well-defined structure and subsequent function of mineralized tissues[5]. This process is based on a highly dynamic environment regulated by an organic matrix that nucleates and directs the hierarchical growth and morphogenesis of mineralized tissue[5]. The charge[6], conformation[7], supramolecular assembly[8], and post-translational cross-linking[9] of specific macromolecules of the organic matrix play key multifunctional roles during the biomineralization process. For example, negatively-charged domains in non-collagenous[10] and non-amelogenin[7] proteins are known to stabilize crystal nucleation while the degree of collagen cross-linking in bone is known to affect its mineral density, microarchitecture, and stiffness[11].

Tissues such as bone and nacre have motivated the development of synthetic mineralizing materials[12]. For example, several research groups have investigated ways to mineralize collagen intrafibrillarly in order to mimic the natural mineralization process of bone tissue[13]. Others have reported materials that resemble the hierarchical structure and chemical composition of nacre using a β-chitin matrix[14] and layer-by-layer polyelectrolyte-clay

dispersions[15]. A particularly inspiring challenge has been, and continues to be, the pursuit of approaches that can recreate the distinctive apatite composition, hierarchical architecture, and corresponding properties of enamel[16]. Towards this goal, Yamagishi *et al.*[17] and Chen *et al.*[18] have developed inorganic chemical methods to grow aligned enamel-like apatite nanocrystals on dental enamel. However, approaches based on organic matrices offer the possibility to guide mineralization through a more biomimetic route based on tuneable organic-inorganic interactions[19]. Pioneering work by Moradian-Oldak *et al.* using amelogenin[20] and Kniep *et al.* using gelatin[21] has enabled the growth of aligned apatite nanocrystals directly on enamel surface. Nonetheless, the development of organized apatite nanocrystals with the distinctive hierarchical order of enamel expanding from the crystallographic-, nano-, micro-, and macro-scale, is still an exciting, yet unattained, goal[20].

There is growing evidence that intrinsically disordered proteins (IDPs) play a fundamental role in mineralization[22]. IDPs contribute in intermolecular interactions at the protein–mineral interface[23]. For example, Beniash *et al.*[24] reported that amelogenin, a highly conserved IDP, undergoes a conformational change from disordered random coils into ordered β-sheet structures, upon interaction with the developing enamel crystals. This conformational change is known to guide crystal growth in enamel formation[25]. Recently, Habelitz *et al.*[26] demonstrated that the distinctive hierarchical structure of mature enamel may require further conformational organization of amelogenin into amyloid-like nanoribbons. Synthetic mineralization platforms that can emulate features of these dynamic supramolecular matrices, exhibiting disorder-order optimization, may lead to the design of materials capable of recreating the structure and properties of biomineralized tissues[12,22].

Elastin-like recombinamers (ELRs) are recombinant macromolecules based on the natural elastin recurrent motif Val-Pro-Gly-X-Gly (VPGXG), where X can be any amino acid apart from proline[27,28]. These biopolymers have generated great interest due to their biocompatibility, biodegradability, and capacity to be synthesized with a high level of molecular control[27]. In addition, ELRs can also serve as models of IDPs[29], where their degree of disorder and order could be controlled to design supramolecular matrices that generate new functionalities[30,31] and potentially guide mineralization. Recently, we have reported that intrinsically-disordered ELRs can stabilize a precursor single crystal phase (brushite), which template the growth of a polycrystalline phase (apatite)[32]. A similar behavior is exhibited by other IDPs in biomineralization[33]. Here, we report the discovery and development of a process that exploits disorder-order interplay of ELRs to guide mineralization with remarkable control and hierarchy. The process enables the fabrication and tuneability of crystallographically aligned apatite nanocrystals. Those nanocrystals are organized into microscopic prisms, which grow together into well-defined macroscopic structures that can populate large volumes. The material exhibits high stiffness, hardness, and acid resistance and can be fabricated as fully mineralized membranes or coatings over uneven surfaces including native tissues.

Results

ELR molecules and self-assembly. Our process is inspired by the current understanding of dynamic organic matrices in biomineralization. We exploited recombinant technologies to design a supramolecular matrix that is based on a molecule that comprises both intrinsically disordered regions and negatively charged domains. The main molecule used is an ELR consisting of a main hydrophobic framework (VPGIG), a positively charged segment (VPGKG) with the amino acid lysine (K) for ELR cross-linking, and the highly-acidic

statherin-derived analogue DDDEEKFLRRIGRFG (SN_A15). Despite the fact that salivary statherin strongly binds to hydroxyapatite and inhibits mineral growth[34], the SN_A15[35] segment comprised of 15 amino acids situated at its N-terminal (DDDEEKFLRRIGRFG) is known to promote mineralization[36,37]. In addition, collagen membranes, ELR-coated glass, and membranes made from similar ELR molecules without the statherin-derived peptide or with the cell adhesive RGDS were used as controls (Supplementary Table 1). When the ELR molecules are dissolved in anhydrous dimethylformamide (DMF) and dried at room temperature while cross-linked using hexamethyl diisocyanate (HDI), they self-assemble into a dense network of β-amyloid-like fibrils (Figure 1a-b-c-d-e) and homogenously distributed three-dimensional (3D) ELR spherulites (Figure 1f-g). On the other hand, no spherulites were observed on the collagen membranes (Supplementary Figure 1). Therefore, these organic supramolecular structures formed independently of the type of ELR used. This result suggests that the formation of spherulites is not dependent on the bioactive sequences nor the molecular weight of the ELRs, but on their VPGIG and VPGKG tropoelastin motifs.

Protein-mediated mineralization process. Upon incubation in a solution supersaturated with respect to fluorapatite at physiological conditions and ionic concentrations, a mineralization process developed within the bulk of the ELR membranes (Supplementary Figure 2). This process resulted in the growth of distinctive hierarchically-ordered mineralized structures (Figure 1h-i-j-k) on both sides of the membranes (Supplementary Figure 3). These structures appeared to emanate from the ELR spherulites within the membrane independently of the ELR used. However, a higher number of mineralized structures were observed on membranes made from the statherin-derived ELR, suggesting that nucleation is enhanced with the quantity of acidic amino acids present within the ELR molecule[35-38] (Supplementary Figure 4). In addition, the structures were not observed on the

collagen membrane controls, while the ELR-coated glass surfaces only comprised flat platelet-like crystals (Supplementary Figure 5).

Surface physical and chemical characterization. The mineralized structures exhibit a spherulite-like morphology with distinctive hierarchical architecture (Figure 1k-l). At the crystallographic length-scale, the material is apatitic in the form of elongated nanocrystals of on average 85.0 ± 22.0 nm thick. At the microscale, these crystals are organized further into prisms with an average diameter of 3.8 ± 0.9 μm and tens of microns in length. These microstructures grow radially into circular structures that can reach up tens of microns in height and 1 mm in diameter (Supplementary Figure 6) while coming together, interlocking (Figure 1m), and populating large uneven areas. This hierarchical mineralization process can produce membranes that are fully mineralized not only on the surface but also throughout their cross-section (Figure 1n).

Rietveld refinement of X-ray diffraction (XRD) data demonstrated that the crystalline phase of the structures matches fluorapatite with a space group, unit cell size, and structural parameters matching fluorapatite values, as reported in the literature (Figure 1o and Supplementary Note 1). This crystalline phase was confirmed by ^{19}F MAS-NMR spectra[39], which verified the presence of a fluorapatite peak at -103 ppm and a fluorite (CaF_2) peak at -108 ppm (Figure 1p). The presence of the organic ELR matrix seemed to promote the formation of fluorapatite phase at the expense of the undesirable fluorite phase, which is beneficial for potential biomedical applications[39]. Furthermore, Fourier Transform Infra-Red (FTIR) spectroscopy analysis revealed spectra that exhibited non-stoichiometric apatite peaks after mineralization in co-existence with the amide peaks (corresponding to the ELR material) (Supplementary Figure 7). In addition, energy dispersive X-ray (EDX) spectroscopy

point and mapping spectra also indicated the presence of calcium, phosphorus, and fluoride (Supplementary Figure 7) with atomic ratios similar to apatite crystals and dental hard tissues[40]. Furthermore, the process enabled the formation of similar hierarchical structures but without the use of fluoride (Supplementary Figure 8).

To demonstrate the functionality of the hierarchical structures, we characterized the mechanical properties by nanoindentation tests (Figure 1q). The structures exhibited a Young's modulus (E) of up to 33.0 ± 20.1 GPa and hardness (H) of up to 1.1 ± 0.8 GPa. The hierarchical structures' E and H are higher than values reported for bone (E = 22.5 ± 1.3 GPa, H = 0.5 ± 0.2 GPa)[41] and dentin (E = 19.4 ± 1.7 GPa, H= 0.5 ± 0.02 GPa)[42] and nearly half of the values reported for dental enamel (E = 72.7 ± 4.5 GPa, H = 3.3 ± 0.3 GPa)[16]. However, it is important to mention that E and H for dental enamel can vary between 50 - 120 GPa and 2.5 - 6 GPa, respectively; depending on the crystal orientation, area within the tissue tested, technique used, and storage conditions[43,44].

Bulk characterization. Throughout the cross-section of the mineralized membranes, scanning electron microscopy (SEM) observations revealed the abundant presence of two types of structures. First, a dense pattern of spherulite-like structures with a granulated central region (Figure 2a-b), which is likely associated with the observed birefringence. Some of these ELR spherulitic structures were mineralized and appeared to template the growth of fluorapatite spherulites made from nanocrystals similar to those observed on the hierarchical structures present on the surface of the membrane (Figure 2c). Second, near the membrane surface, mineralized structures with nanocrystals were oriented at 78 ± 6º with respect to the membrane surface and appeared to grow vertically towards the surface of the membrane (Figure 2d and Supplementary Figure 9). Interestingly, density-dependent colour SEM

(DDC-SEM), which simultaneously enables topographical and density assessment, revealed a thin low-density material (green) surrounding a denser (orange) one on both of these structures. According to the EDX spectral mapping, the less dense material was found to be rich in carbon, oxygen, and nitrogen, which are commonly found in organic materials. In contrast, the denser material exhibited an abundance of calcium and phosphorus, reflecting its inorganic nature and suggesting an intimate organic-inorganic interaction (Figure 2e-f and Supplementary Figures 10-11-12).

SEM analysis using the backscattered electron mode (BSE) revealed that the centers of the hierarchical mineralized structures comprised mineralized cores deep within the bulk of the membrane (Figure 2g-h, Supplementary Figure 13, and Supplementary Movies 1-2). As the hierarchical structures spread radially on the surface, the nanocrystals in closer proximity to the ELR matrix changed their orientation gradually from parallel to the surface towards the inside of the membrane (Fig 2i-j). This behavior suggests a preference of the nanocrystals to grow within the ELR matrix. To further investigate this preferential growth and crystallographic orientation of the nanocrystals, ultrathin sections were milled via focused ion beam (FIB) and analyzed by high resolution transmission electron microscopy (HRTEM) and selected area electron diffraction (SAED) (Figure 2k-l-m, and Supplementary Figure 14). The results demonstrate that the nanocrystals within the ELR matrix display a flat geometry at the end of their *c*-axis (Supplementary Figure 15). In contrast, nanocrystals exhibiting a needle-like morphology have been associated with mineralization processes that do not rely on organic matrices to regulate their growth[18]. This offers further evidence that the ELR not only interacts at the basal plane of the fluorapatite crystals but also provides an optimum environment for their growth front within the matrix.

In addition, Fast Fourier Transform (FFT) analysis of the HRTEM images reveals that the nanocrystals are preferably oriented so that the *a*-axis is perpendicular to the growth direction. Nanocrystals have a co-alignment of several degrees ranging between 7-10°, which may contribute to the spherulitic radial geometry of the hierarchical structures as seen in examples of other biomineralization systems[45] (Figure 2n and Supplementary Figure 16). These results demonstrate that ELR spherulites within the bulk of the membrane act as supramolecular organic frameworks that interact intimately with apatite crystals and template their growth into hierarchical mineralized structures.

Tuneability of the process. A major advantage of the process is the possibility to use and tune disorder-order interplay of the ELR molecules to design complex supramolecular organic environments that can control mineralization[22,46]. Through FTIR deconvolution of the amide III spectral region, a quantitative analysis of the protein secondary structure can be established[47]. We discovered that by systematically modifying the amount of cross-linker, it was possible to modulate the levels of ELR ordered β-sheet and disordered random coil conformation, while maintaining β-turn and α-helix nearly constant (Figure 3a-b, Supplementary Figure 17, and Supplementary Table 2). In other words, tuning the amount of ELR cross-links during solvent evaporation enabled controlled access to different ELR disorder-order ratios within the resulting membrane. Using this drying/cross-linking approach, we found that it was possible to control the formation of ELR spherulites. When the ratio of disordered (random coil) to ordered (β-sheet) secondary structure (random : β ratio) was kept below 0.26 ± 0.06, no spherulites were formed. However, by gradually increasing the level of random coil (random : β ratios of 0.44 ± 0.02, 0.87 ± 0.03, and 1.05 ± 0.17), we were able to control the formation and number of ELR spherulites (0.17, 3.24, and

up to 5.38 spherulites/mm^2, respectively) (Figure 3c(I)), demonstrating that ELR disorder-order optimization can be used to generate organic matrices with supramolecular control.

By modulating the ELR conformation in this manner, it appeared to be possible to tune the structural hierarchy of the mineralized structures and consequently the properties of the resulting material. As the supramolecular organization of the ELR matrix transitioned from a random : β ratio of 0.26 ± 0.06 to 1.05 ± 0.17, the microscale geometry of the hierarchical mineralized structures shifted from concentric rings to radial prisms (Figure 3c (II)). However, independently of the microscale geometry, all structures comprised of aligned nanocrystals but they tended to be denser in softer membranes (made with lower amount of cross-linker) compared to stiffer ones (made with higher amount of cross-linker). This control of the nanocrystal density enabled the possibility to tune both the Young's modulus (E) and hardness (H) of the mineralized structures. Structures grown within softer membranes exhibited higher E (33.0 ± 20.1 GPa) and H (1.1 ± 0.8 GPa) compared to structures grown within moderate (E = 17.7 ± 11.3 GPa, H = 0.8 ± 0.3 GPa) and stiff (E = 8.2 ± 1.4 GPa and H = 0.6 ± 0.1 GPa) membranes. This increase in mechanical properties of the hierarchical mineralized structures on softer ELR membranes may result from the nanocrystals more easily displacing the ELR matrix and growing in closer proximity to each other. However, independently of the microstructure generated, the chemical composition remained the same (Supplementary Figure 18). These results demonstrate the capacity to program the hierarchical structure and resulting properties of the mineralized material by modulating disorder-order levels of the ELR organic matrix. We speculate that this possibility is in agreement with the increasingly recognized importance of IDPs in biomineralization[22]. Furthermore, these findings may provide insights into the role of IDPs in pathological mechanisms such as diseases of the central nervous system[48] or cardiovascular calcification[49].

The process can also be tuned by modulating other processing parameters. For example, increasing the number of negatively charged acidic domains within the ELR molecule/spherulite, such as those found in statherin-ELR, led to a higher number of mineralized structures. Also, controlling the kinetics of ionic consumption by maintaining a constant pH during the mineralization process considerably increased the size of the hierarchical structures up to a millimeter in diameter. Nonetheless, is important to highlight that hierarchical structures can also be formed in physiological ionic concentrations (2.5 mM Ca^{2+}, 1.5 mM PO_4^{3-}) (Supplementary Figure 19).

Mechanism of formation. Based on our data, we propose the following mechanism of I) ELR matrix assembly and II) calcium phosphate (CaP) nucleation and growth of the mineralized structures (Figure 4).

ELR matrix assembly. The protein-mediated mineralization process relies on the hydrophobic (VPGIG)/hydrophilic (VPGKG) block structure and disordered nature of the ELR molecules. In this first stage, during cross-linking, the ELR molecules organize into β-amyloid-like fibres, as previously predicted[50], and spherulitic structures with the characteristic Maltese-cross pattern upon drying. As the DMF solvent evaporates, the ELR self-assembles transitioning from being random (disordered) in the DMF solution[51] into a β-sheet conformation (ordered) in dry state. While drying is known to induce molecular order[52] (β-sheet conformation in our case), cross-linking prevents it by decreasing the molecule's entropy, as evidenced by progressively inducing random coil by gradually increasing levels of cross-linking. In this way, the organic matrix can be easily modulated to systematically access different disorder-order compositions as well as different organizations of ELR

spherulites. This is a critical capability of our process because, while the specific mechanism for the formation of protein-based spherulites remains vague[53], it is known that these structures grow by triggering radially oriented crystalline regions located between amorphous chains[54]. Our approach enables the formation and modulation of these disordered-ordered regions. Furthermore, while proteins are known to form spherulites[55], to our knowledge, this is the first time that a recombinant elastin protein has been reported to form such supramolecular structures.

CaP nucleation and growth of mineralized structures. The 3D ELR spherulites within the matrix (membrane) then act as nucleating and templating sites for mineralization as CaP ions from the mineralization solution diffuse through the membrane. Membranes with a higher number of ELR spherulites comprised more mineralized structures (87.5 structures/mm^2) while those with a lower number of ELR spherulites comprised less mineralized structures (25.1 structures/mm^2). After nucleation, we propose that the rich ELR spherulites begin to template the growth of apatite nanocrystals and evolve into mineralized spherulites. This templating may be facilitated by the structural disorder of the ELR matrix, enabling both random and β structures, reported previously[22,26].

ELR spherulites are formed within the cross-section of the ELR matrix and, like polymeric spherulites, grow until they meet adjacent ones. The spherulites located closer to the surface of the membrane have fewer limitations to grow towards and on the surface of the membrane. In this way, mineralized structures templated by ELR spherulites closer to the surface of the membrane not only have open space to grow but also more access to CaP ions. Once on the surface, the mineralizing structures continue to spread until they meet others. Despite changes in the microscale architecture of mineralized structures growing on membranes with different

amounts of cross-linking, the outward alignment of the nanocrystals remains the same, suggesting that the microscale organization is at least in part dependent on the properties of the matrix. To explore this, we used a model based on the wrinkling of a thin circular annulus (represented by the hierarchical mineralized structure) supported by elastic foundations (represented by the underlying ELR matrix)[56]. The bending stiffness of the mineralized structures in the principal direction becomes negligible and would respond with a circumferential out-of-plane deflection (the wrinkles) when radial compressive loads (as a result of the radially outward nanocrystal growth) are applied to either the inner or outer edge. In this scenario, the model predicts that softer ELR membranes would generate wrinkles with circular symmetry (the ring morphology) while stiffer ELR membranes would generate wrinkles with radial symmetry (i.e. prismatic morphology) (Supplementary Figure 20). It is also important to mention that differences in ionic diffusion across the membrane as a result of the various conformations of the ELRs may also play a role in the morphology of the mineralized structures (Supplementary Table 3)[57].

Our approach takes advantage of the disordered nature of ELR molecules to trigger a supramolecularly organized organic framework capable of controllably templating the growth of apatite crystals at multiple length scales. This mechanism goes beyond biomimicry and opens up the possibility to not only modulate mineralization but also to explore ways of utilizing disorder-order interplay for the generation of functional materials.

Application in dental tissue repair. Hierarchical structures play a key role in mineralized tissues such as bone, dentin, and enamel. In particular, dental enamel offers a unique structure/function relation (Figure 5a-c-e), which has not yet been recreated[16]. Given, the vast clinical need and potential impact of engineering more efficient materials to replace

lost/diseased enamel, we conducted *in vitro* proof-of-concept studies to investigate the potential use of the hierarchical mineralized structures (Fig. 5b-d-f) for dentin hypersensitivity as a mineralizing bandage to occlude exposed dentinal tubules.

Membranes were fabricated directly on both etched and rough surfaces of human dentin and mineralized for 8 days. SEM observations confirmed that the hierarchically mineralized membranes grew, adhered, and conformed to the surface of the etched dental tissues (Figure 6a-b-c). Integration between the hierarchical structures and the dental tissues was observed at the dentin-membrane interface, where the nanocrystals infiltrated and blocked dentinal tubules (Figure 6d). Furthermore, to assess the acid resistance of the mineralized coatings, we conducted acid attack experiments, on both mineralized membranes and dental enamel. The mineralized structures exhibited comparable acid resistance to dental enamel after 15 minutes of exposure (Figure 6e-f). It is probable that the acid resistance exhibited by the mineralized structures is related to their intrinsic fluorapatite crystalline phase in comparison to the carbonated hydroxyapatite phase found in enamel[58]. As expected, after 7 days of exposure to acid, the inorganic content of the mineralized membranes and dental enamel were disturbed. Interestingly, the stiffness of ELR membranes after the 7-day acid attack was similar to that of unmineralized membranes, suggesting that the ELR matrix was preserved after the attack (Supplementary Figure 21). This preservation could potentially enable a remineralization treatment once the acid attack subsides. However, confirmation of this hypothesis would require further experimentation, which is beyond the scope of the current study. Another potential challenge encountered by dental tissues is exposure to proteases in saliva[59]. Therefore, membranes were tested for enzymatic degradation by elastase exposure. DDC-SEM observations confirmed the presence of the nanocrystals (high-density material) and a reduction of the low-density material (organic matrix) (Figure 6g). This result demonstrates

that the prismatic structures can maintain their organization in spite of the reduction of the organic matrix around them. Great progress has been made aiming to repair enamel using either wet chemical processes[18] or organic matrices[20,21]. Our process provides a potential route to control the growth of fluorapatite crystals with tuneable hierarchical order and mechanical properties.

Discussion

This work demonstrates the possibility to use IDPs to modulate disorder-order ratio to program mineralization. The process is based on a tuneable supramolecular organic matrix that enables the growth of aligned nanocrystals into hierarchical mineralized structures. These materials exhibit high stiffness, hardness, and acid resistance and can be fabricated as fully mineralized membranes or coatings over uneven surfaces including native tissues. In addition, the simplicity and versatility of the mineralization platform opens up opportunities to tackle regenerative challenges of mineralized tissues. Furthermore, the work not only introduces an exciting strategy to design and grow materials, but also provides insight into phenomena emerging from disorder-order optimization. As such, our study is highly relevant for different fields including for example materials science, biomineralization, and structural biology.

Acknowledgements

The work was supported by the ERC Starting Grant (STROFUNSCAFF), The Marie Curie Integration Grant FP7-PEOPLE-2013-CIG (BIOMORPH), Institute of Bioengineering, Life Science Initiative, and QMUL studentships. J.C.R.C. acknowledges the support from EC (HEALTH-F4-2011-278557, PITN-GA-2012-317306, MSCA-ITN-2014-642687 and NMP-2014-646075), MINECO (MAT2013-42473-R and MAT2015-68901R) and JCyL

(VA244U13, VA313U14 and VA015U16). N.M.P. is supported by the European Research Council PoC 2015 “Silkene” no. 693670, by the European Commission H2020 under the Graphene Flagship Core 1 no. 696656 (WP14 “Polymer Nanocomposites”) and FET Proactive “Neurofibres” grant no. 732344. The authors would like to thank Prof. Robert Hill, Dr Natalia Karpukhina and Prof. Alan Boyde at Centre of Oral Growth and Development, QMUL (UK) for valuable discussions, and Mr Russell Bailey at the Nanovision, QMUL for technical support. The authors thank Miss Rebecca Carroll (QMUL) for her excellent support during the histological sample preparation. We would like also to thank Dr Harold Toms at the School of Biological and Chemical Science, QMUL (UK) for his help during the MAS-NMR study. The authors would also like to acknowledge Dr Benjamin Robinson at Imperial College London for his constructive discussions during AFM experiments.

Author contributions

S.E., M.A.J, A.M. conceived the project. S.E. carried out the experiments. M.A.J. and A.M. supervised the study. S.E., H.J., K.M. and E.T.M. fabricated the ELR membranes used in this study. M.A. and J.C.R.C. provided the ELRs. K.S. conducted the experiments on the ELR-coated glasses. A.J.B., S.E. and K.S. performed and analyzed FIB-SEM data. S.E. and R.M.W. collected and analyzed the XRD data. S.E. and K.M. performed the cross-linking studies. S.E. and N.V.T. performed the TEM experiments, analyzed TEM images and SAED patterns. S.A., S.E, A.M, and M.M.S. planned and conducted the DDC-SEM imaging. S.E., A.R., A.D.R.H., A.M. planned, conducted and analyzed AFM data. S.E., A.M., M.F.P., and N.M.P. planned, conducted, and interpreted the nanoindentation experiments. S.E. and H.J. conducted the polarized light microscopy experiments. E.B., S.E., and A.M. conducted the modelling for the hierarchical structures S.E. and A.M. interpreted the data and wrote the manuscript. All authors discussed the results and commented on the manuscript.

Additional information

Supplementary Information accompanies this paper at http://www.nature.com/naturecommunications.

Competing financial and non-financial interests

The authors declare no competing interests.

Methods

Membrane fabrication and ELR glass coating. Membranes were fabricated by dissolving different ELR molecules as shown in (Supplementary Table 1) in anhydrous dimethylformamide (DMF) at room temperature in a low-humidity conditions (less than 20%) inside a polymer glove box. Then the resultant solution was cross-linked using hexamethyl diisocyanate (HDI), drop-casted on top of PDMS substrate, left to dry overnight, and then washed with deionized water for three days and stored at 4ºC. Systematic processing variations in order to control the stiffness/ELR conformation of the membranes by changing the cross-linker to lysine ratios (0.25, 0.5, 1, 3, 6, and 12). Collagen membranes processed as above, were used as controls. Similar fabrication procedures were undertaken to fabricate membranes on the dentin substrates. For ELR glass coating, 100 µg of ELR was dissolved in deionized water and drop-casted onto the borosilicate glass substrates, and left to dry. After drying the membranes were observed under polarized light microscope with a cross-polarizer to check the formation of ELR spherulites.

Enamel and dentin discs preparation. Extracted human non-carious teeth (with approval from Queen Mary Research Ethics Committee QMREC2008/57) were stored at 4ºC in

deionized water refreshed every 7 days until needed. Each tooth was carefully mounted on a holder and placed inside the diamond cut-off machine (Accutom-5, Struers A/S, Ballerup, Denmark) by aid of a compound material, the required X and Y starting positions along with Y stop position were selected and saved. Teeth were cut across their axes into discs, the thickness of each dentin disc was about 500 µm. The tooth sections were carefully polished using a polishing unit (Kent 4, automatic lapping and polishing unit) by aid of silicon carbide (SiC) grinding papers (CarbiMet^{TM}) from coarse to fine as follows (P600, P1000, P2500, and P4000). Subsequently, the samples were polished using polishing cloth and diamond suspension waterbase (Metprep^{TM}) as follows (3, 1, and 0.25 µm). Finally, the dentin discs were acid etched using 6% citric acid for 2 minutes[60]; however, enamel samples (longitudinal sections) that were used as controls for SEM images were etched using 38% phosphoric acid for 30 seconds[61]. Then the ELR membranes were fabricated *in situ* on top of the dentin discs was conducted.

Crystal growth experiment. 2 mM of hydroxyapatite powder and 2mM of sodium fluoride were added to 100 ml of deionized water with continuous stirring. Subsequently, 69% nitric acid was added dropwise into the solution slowly until the powder was completely dissolved. 30% ammonium hydroxide solution was added dropwise until the pH was readjusted to 6.0[62], and then different ELR membranes were placed at the bottom of beaker and incubated for eight days at 37 ˚C using a temperature-controlled incubator (LTE Scientific, Oldham, UK). Furthermore, initial ionic strength was varied to mimic natural saliva at concentrations of 2.5 mM and 1.6 mM of calcium and phosphate, respectively. Quantification and analysis of the mineralized structures were conducted by ImageJ.

SEM, DDC-SEM, and EDX spectroscopy. Samples were mounted after being dried on aluminum stubs via self-adhesive tape and were coated using an auto sputter coating machine with a conductive material. Samples were analyzed using an FEI Inspect F (Hillsboro, OR, USA). Their surface topography was observed using a secondary electron detector. A backscattered electron (BSE) detector was used to assess the variation in density within each sample. Furthermore, the elemental analysis was carried out using INCA software. Point and mapping spectra collection at areas of interest were carried out using an EDX detector (INCA x-act, Oxford Instruments) at an accelerating voltage of 10 kV. In other instances, samples were investigated using SEM (Gemini 1525 FEGSEM), operated at 10 kV. The instrument was equipped with both an inlens detector that recorded secondary electrons, and a backscatter electron detector. The DDC-SEM images were obtained by imaging the same region with both inlens mode and backscatter mode. Using ImageJ software, both images were stacked and the inlens image was assigned to the green channel whereas the backscatter image was assigned to the red channel[63].

Focused ion beam-scanning electron microscopy. Focused ion beam-scanning electron microscopy (FIB-SEM) was undertaken using an FEI Quanta 3D ESEM (Hillsboro, OR, USA) for which the gallium ion beam parameters were set to 30 kV and 1 nA in order to cut trenches from the mineralized structures. Areas to be milled on the samples were selectively protected from the gallium source by depositing 2 µm of platinum coating. For the 3D reconstructed data, mineralized structures were milled, where each slice was 73 µm wide, 65 µm tall and 20 µm deep, while the images were captured at 5 kV with magnification of 4000x after each cut using auto slice and view software (FEI) with resolution of 1024x884 were then reconstructed using ImageJ (National Institute of Health, USA) and Drishti (Australia National University, Canberra, Australia) softwares[64]. TEM specimens were prepared using a

FEI Quanta 3D ESEM by focused Ga+ ion beam milling. The wedge cut technique followed by an in situ welding lift-out and thinning was applied. Thinning using a 30 kV ion beam and currents down to 28 pA was done from both sides of the specimen at a 2° incidence angle until the lamella was about 150 nm thick. The final low-kV cleaning was performed at 16 kV, 28 pA and 1° incidence angle.

Histological characterization. ELR membranes were embedded in paraffin wax blocks, cut into sections of about 3 µm, and stained with Congo Red and Elastin Von Gieson to visualize under optical light microscope its amyloid and elastin content respectively.

Attenuated total reflection Fourier transform infra-red spectroscopy (ATR-FTIR). FTIR analysis was conducted using the FTIR Spectrum GX (PerkinElmer®, Waltham, MA, USA). Membranes before and after mineralization were properly secured over the IR window before scanning equipped with ATR attachment. Human non-carious dental enamel powder (kindly supplied by Prof. Colin Robinson, University of Leeds) was also analyzed for comparison purposes. The program was set to take the average of 128 scans at resolution of 4 cm^{-1} after subtracting the background, and were analyzed at a wavenumber of 4000 cm^{-1} to 450 cm^{-1} in respect to % of transmittance and % of absorbance for inorganic and organic samples respectively. Usually, amide I spectral region (1700 – 1600 cm^{-1}), is most commonly used to detect the secondary structure of proteins because of its strong signal, while it has several limitations, including a strong interference from water vibrational band, relatively unstructured spectral contour, and overlap of revolved bands correspondingly to various secondary structures. In contrast, amide III that was investigated in our study, at spectral region (1350 – 1200 cm^{-1}), even if relatively weak in signals, does not have the above limitations. Easily resolved and better defined amide III bands are suitable for quantitative

analysis of the protein secondary structure. By using Origin software, amide III region has been successfully deconvoluted and used for determination of α-helix and β-sheets, bands corresponding to β-turns and random coils. The assignments of spectral bands were as follows: 1220 – 1250 cm^{-1} for β-sheets, 1250 – 1270 cm^{-1} for random coils, 1270 – 1295 cm^{-1} for β-turns, 1295 – 1330 cm^{-1} for α-helix[47].

X-ray diffraction (XRD). Powder diffraction was conducted at room temperature to elucidate the phase composition of the mineralized membrane, using an X'Pert Pro X-ray diffractometer (PANalytical, B.V., Almelo, Netherlands) with flat plate θ/θ geometry and Ni-filtered Cu-Kα radiation at 45 kV and 40 mA, where Kα1 and Kα2 equal 1.540598 and 1.5444260 Å respectively. The 2θ range of the diffraction pattern was taken from 5 - 70˚ with a step size 0.0334˚ and data was collected continuously with an equivalent step time of 1600 seconds using a PANalytical X'Celerator solid-state RTMS detector. Rietveld modelling was performed using X'pert highscore (3.0e) with the ICDD PDF-4+ database for 2014[65].

^{19}F magic angle spin-nuclear magnetic resonance (^{19}F MAS-NMR). In order to investigate the fluoride interactions present in both the powder collected from base of the beakers with no ELR membranes (as a control) and the mineralized membranes, all samples were crushed into fine powder using pestle and mortar, and then analyzed. Solid-state ^{19}F MAS-NMR analysis was conducted using a 14.1 Tesla spectrometer (600 MHz Bruker, Coventry, UK) at a Larmor frequency of 564.5 Mega Hertz (MHz) under spinning conditions of 22 kHz in a 2.5 mm rotor. The spectra were acquired from a single-pulse experiment of 60 seconds recycle duration, by using a fluorine free background probe. The ^{19}F chemical shift scale was calibrated using the -120 ppm peak of 1M of NaF solution along with trichloro-fluoro-methane ($CFCl_3$), as a second reference. Spectra were acquired for 4 hours with accumulation

of 240 scans, while for the protein membranes there was an accumulation of 4 runs each for 4 hours.

Transmission electron microscopy (TEM). Transmission electron microscopy was performed on the FIB-prepared lamellas using a JEOL JEM 2010 (JEOL Ltd., Tokyo, Japan) operated at 120 kV. The obtained images were analyzed using the Gatan Microscopy Suite® (GMS 3) software. For the analysis of crystal phases present in the samples, d-values obtained from SAED patterns were compared with d-values obtained from the same samples using XRD measurements and the Powder diffraction file - PDF2 database (ICDD, USA, release 2009).

Atomic force microscopy (AFM) nanoindentation. Unmineralized samples were attached to a petri dish using a drop of cyanoacrylate adhesive, and left for a minute for the adhesive to dry. Samples were then immersed in distilled water. Young's modulus measurements were taken with a JPK Nanowizard-1 (JPK Instruments, Germany) in force spectroscopy mode, mounted on an inverted optical microscope (IX-81; Olympus, Japan). Quadratic pyramidal cantilevers (MLCT; Bruker, MA, USA) with a spring constant of 0.07 N/m and half-angle to face of 17.5º were used for indentation. The sensitivity of cantilevers was determined before measurements by measuring the slope of the force-distance curve in the AFM software on an empty region of a petri dish. Indentation was carried out with an approach speed of 5 µm/s and a maximum set force of 1 nN. Measurements were taken multiple times per region and in multiple regions per sample. The Young's modulus was calculated by fitting the contact region of the approach curve with the Hertz Contact model[66] using the JPK software, using the above constants and calibrated cantilever sensitivity. Graphs were plotted with GraphPad Prism software, using a P value of 0.05.

Young's modulus and hardness measurements. Before the measurements, the nanoindenter was calibrated against a reference sample that was fused silica in our case, as suggested by the machine supplier. Calibration was performed using the same method that was then implemented for tests on dental and membrane samples. Mineralized membrane samples were glued flat onto an aluminum holder. Enamel samples were put into a mold filled with fluid resin. After resin curing, enamel samples were polished in order to have a flat surface where to perform the mechanical tests. Nanoindentation tests were carried out through a nanoindenter (iNano) by Nanomechanics, Inc. (maximum indentation load of 50 mN), that was used in dynamic mode in order to monitor the variation of the young's modulus and hardness as a function of the indentation depth. In order to reduce the influence of the soft underneath membrane on the mechanical properties of mineralized samples, we considered the mechanical properties measured at the outmost surface, which corresponds to an indentation depth of 30 nm.

Ionic strength measurements. The concentration of calcium and fluoride ions in the mineralizing solution was analyzed using an ion□selective electrode (ISE) in combination with a potassium nitrate reference electrode (ELIT Ion Analyser, Nico 2000 Ltd, Harrow, UK), four channel ion analyzer and computer interface software. The ISE was calibrated by standard solutions within the concentration range employed for both calcium and fluoride. A straight line of mV versus concentration plotted to provide the calibration data.

Acid attack experiments. Both human dental enamel and mineralized membranes were subjected to 0.1 M of acetic acid adjusted to pH 4.0 and incubated at 37ºC for different timepoints[67].

583

584 **Enzymatic digestion.** Mineralized membranes were subjected to elastase (from hog pancreas
585 source) digestion[68] after optimization of the concentration adjusted to 15 U/ml for 72 hours at
586 37ºC.

587

588 **Swelling measurements.** Swelling measurements to yield diffusion coefficient values at
589 different cross-link densities. A circle was punched out of each ELR membrane (different
590 cross-link densities) using a 0.5cm biopsy punch. The dry weight and dimensions of each
591 membrane were then recorded using a micro-balance and micrometer. Each membrane was
592 immersed in a petri dish full of deionized water. The petri dish was placed under an optical
593 microscope with a calibrated scale. The diameter and thickness of the membrane were
594 measured as a function of time over the following time points: at 30 second intervals from 0 -
595 10 minutes, at 10 minute intervals from 10 - 60 minutes, at 60 minute intervals from 60 - 480
596 minutes and at 24 hour intervals between 480 - 2880 hours. The moment the membrane was
597 placed inside the petri dish was taken as t = 0. These measurements were carried out at room
598 temperature**.** Analyses and calculations were conducted using ImageJ implementing Tanaka
599 and Fillmore equations[69].

600

601 **Data availability.** The data that support the findings of this study are available from the
602 authors on reasonable request, see author contributions for specific data sets.

603

604 **References**

605 1 Wegst, U. G. K., Bai, H., Saiz, E., Tomsia, A. P. & Ritchie, R. O. Bioinspired
606 structural materials. *Nature Materials*, 23-36 (2014).
607 2 Lakes, R. Materials with structural hierarchy. *Nature* **361**, 511-515 (1993).
608 3 Weiner, S. & Addadi, L. Design strategies in mineralized biological materials.
609 *Journal of Materials Chemistry* **7**, 689-702 (1997).

4 Aizenberg, J. & Fratzl, P. Biological and biomimetic materials. *Advanced Materials* **21**, 187-188 (2009).

5 Addadi, L. & Weiner, S. Control and Design Principles in Biological Mineralization. *Angewandte Chemie International Edition in English* **31**, 153-169 (1992).

6 Naka, K. & Chujo, Y. Control of crystal nucleation and growth of calcium carbonate by synthetic substrates. *Chemistry of Materials* **13**, 3245-3259 (2001).

7 Fan, D., Lakshminarayanan, R. & Moradian-Oldak, J. The 32 kDa enamelin undergoes conformational transitions upon calcium binding. *Journal of Structural Biology* **163**, 109-115 (2008).

8 Fang, P. A., Conway, J. F., Margolis, H. C., Simmer, J. P. & Beniash, E. Hierarchical self-assembly of amelogenin and the regulation of biomineralization at the nanoscale. *Proceedings of the National Academy of Sciences of the United States of America* **108**, 14097-14102 (2011).

9 Kaartinen, M. T., Sun, W., Kaipatur, N. & McKee, M. D. Transglutaminase crosslinking of SIBLING proteins in teeth. *Journal of Dental Research* **84**, 607-612 (2005).

10 Goldberg, H. A., Warner, K. J., Stillman, M. J. & Hunter, G. K. Determination of the hydroxyapatite-Nucleating region of bone sialoprotein. *Connective Tissue Research* **35**, 385-392 (1996).

11 Saito, M. & Marumo, K. Effects of Collagen Crosslinking on Bone Material Properties in Health and Disease. *Calcified Tissue International* **97**, 242-261 (2015).

12 Fratzl, P. & Weinkamer, R. Nature's hierarchical materials. *Progress in Materials Science* **52**, 1263-1334 (2007).

13 Li, Y. *et al.* Biomimetic mineralization of woven bone-like nanocomposites: Role of collagen cross-links. *Biomacromolecules* **13**, 49-59 (2012).

14 Mao, L. B. *et al.* Synthetic nacre by predesigned matrix-directed mineralization. *Science*, 1-9 (2016).

15 Tang, Z., Kotov, N. A., Magonov, S. & Ozturk, B. Nanostructured artificial nacre. *Nature Materials* **2**, 413-418 (2003).

16 Habelitz, S., Marshall, S. J., Marshall G.W, Jr. & Balooch, M. Mechanical properties of human dental enamel on the nanometre scale. *Archives of Oral Biology* **46**, 173-183 (2001).

17 Yamagishi, K. *et al.* A synthetic enamel for rapid tooth repair. *Nature* **433**, 819 (2005).

18 Yin, Y., Yun, S., Fang, J. & Chen, H. Chemical regeneration of human tooth enamel under near-physiological conditions. *Chemical Communications*, 5892-5894 (2009).

19 Palmer, L. C., Newcomb, C. J., Kaltz, S. R., Spoerke, E. D. & Stupp, S. I. Biomimetic systems for hydroxyapatite mineralization inspired by bone and enamel. *Chemical Reviews* **108**, 4754-4783 (2008).

20 Ruan, Q., Zhang, Y., Yang, X., Nutt, S. & Moradian-Oldak, J. An amelogenin-chitosan matrix promotes assembly of an enamel-like layer with a dense interface. *Acta Biomaterialia* **9**, 7289-7297 (2013).

21 Busch, S., Schwarz, U. & Kniep, R. Morphogenesis and structure of human teeth in relation to biomimetically grown fluorapatite-gelatine composites. *Chemistry of Materials* **13**, 3260-3271 (2001).

22 Boskey, A. L. & Villarreal-Ramirez, E. Intrinsically disordered proteins and biomineralization. *Matrix Biology* **52-54**, 43-59 (2016).

23 Delak, K. *et al.* The tooth enamel protein, porcine amelogenin, is an intrinsically disordered protein with an extended molecular configuration in the monomeric form. *Biochemistry* **48**, 2272-2281 (2009).

24 Beniash, E., Simmer, J. P. & Margolis, H. C. Structural changes in amelogenin upon self-assembly and mineral interactions. *Journal of Dental Research* **91**, 967-972 (2012).
25 Fincham, A. G. *et al.* Evidence for amelogenin 'nanospheres' as functional components of secretory-stage enamel matrix. *Journal of Structural Biology* **115**, 50-59 (1995).
26 Carneiro, K. M. M. *et al.* Amyloid-like ribbons of amelogenins in enamel mineralization. *Scientific Reports* **6** (2016).
27 Girotti, A. *et al.* Design and bioproduction of a recombinant multi(bio)functional elastin-like protein polymer containing cell adhesion sequences for tissue engineering purposes. *Journal of Materials Science: Materials in Medicine* **15**, 479-484 (2004).
28 Urry, D. W. *What sustains life?: Consilient mechanisms for protein-based machines and materials*. (2006).
29 Roberts, S., Dzuricky, M. & Chilkoti, A. Elastin-like polypeptides as models of intrinsically disordered proteins. *FEBS Letters* **589**, 2477-2486 (2015).
30 Inostroza-Brito, K. E. *et al.* Co-Assembly, spatiotemporal control and morphogenesis of a hybrid protein-peptide system. *Nature Chemistry* **7**, 897-904 (2015).
31 Simon, J. R., Carroll, N. J., Rubinstein, M., Chilkoti, A. & López, G. P. Programming molecular self-assembly of intrinsically disordered proteins containing sequences of low complexity. *Nature Chemistry* **9**, 509-515 (2017).
32 Shuturminska, K. *et al.* Elastin-like protein, with statherin derived peptide, controls fluorapatite formation and morphology. *Frontiers in Physiology* **8** (2017).
33 Chang, E. P. *et al.* The intrinsically disordered C-RING biomineralization protein, AP7, creates protein phases that introduce nanopatterning and nanoporosities into mineral crystals. *Biochemistry* **53**, 4317-4319 (2014).
34 Raj, P. A., Johnsson, M., Levine, M. J. & Nancollas, G. H. Salivary statherin. Dependence on sequence, charge, hydrogen bonding potency, and helical conformation for adsorption to hydroxyapatite and inhibition of mineralization. *J Biol Chem* **267**, 5968-5976 (1992).
35 Shah, S., Kosoric, J., Hector, M. P. & Anderson, P. An in vitro scanning microradiography study of the reduction in hydroxyapatite demineralization rate by statherin-like peptides as a function of increasing N-terminal length. *Eur J Oral Sci* **119 Suppl 1**, 13-18 (2011).
36 Tejeda-Montes, E. *et al.* Mineralization and bone regeneration using a bioactive elastin-like recombinamer membrane. *Biomaterials* **35**, 8339-8347 (2014).
37 Tejeda-Montes, E. *et al.* Bioactive membranes for bone regeneration applications: Effect of physical and biomolecular signals on mesenchymal stem cell behavior. *Acta Biomaterialia* **10**, 134-141 (2014).
38 Addadi, L., Berman, A., Oldak, J. M. & Weiner, S. Structural and stereochemical relations between acidic macromolecules of organic matrices and crystals. *Connective Tissue Research* **21**, 127-135 (1989).
39 Mohammed, N. R. *et al.* Effects of fluoride on in vitro enamel demineralization analyzed by 19F MAS-NMR. *Caries Research* **47**, 421-428 (2013).
40 Elliott, J. C. Structure, crystal chemistry and density of enamel apatites. *CIBA Foundation Symposia*, 54-72 (1997).
41 Zysset, P. K., Edward Guo, X., Edward Hoffler, C., Moore, K. E. & Goldstein, S. A. Elastic modulus and hardness of cortical and trabecular bone lamellae measured by nanoindentation in the human femur. *Journal of Biomechanics* **32**, 1005-1012 (1999).

42 Kinney, J. H., Balooch, M., Marshall, S. J., Marshall, G. W. & Weihs, T. P. Hardness and young's modulus of human peritubular and intertubular dentine. *Archives of Oral Biology* **41**, 9-13 (1996).
43 Habelitz, S., Marshall, G. W., Balooch, M. & Marshall, S. J. Nanoindentation and storage of teeth. *Journal of Biomechanics* **35**, 995-998 (2002).
44 Cuy, J. L., Mann, A. B., Livi, K. J., Teaford, M. F. & Weihs, T. P. Nanoindentation mapping of the mechanical properties of human molar tooth enamel. *Archives of Oral Biology* **47**, 281-291 (2002).
45 Sun, C. Y. *et al.* Spherulitic Growth of Coral Skeletons and Synthetic Aragonite: Nature's Three-Dimensional Printing. *ACS Nano* **11**, 6612-6622 (2017).
46 Kalmar, L., Homola, D., Varga, G. & Tompa, P. Structural disorder in proteins brings order to crystal growth in biomineralization. *Bone* **51**, 528-534 (2012).
47 Cai, S. & Singh, B. R. Identification of β-turn and random coil amide III infrared bands for secondary structure estimation of proteins. *Biophysical Chemistry* **80**, 7-20 (1999).
48 Chiti, F. & Dobson, C. M. in *Annual Review of Biochemistry* Vol. 75 333-366 (2006).
49 Reznikov, N., Steele, J. A. M., Fratzl, P. & Stevens, M. M. A materials science vision of extracellular matrix mineralization. *Nature Reviews Materials* **1** (2016).
50 Rauscher, S., Baud, S., Miao, M., Keeley, Fred W. & Pomès, R. Proline and Glycine Control Protein Self-Organization into Elastomeric or Amyloid Fibrils. *Structure* **14**, 1667-1676 (2006).
51 Knubovets, T., Osterhout, J. J. & Klibanov, A. M. Structure of lysozyme dissolved in neat organic solvents as assessed by NMR and CD spectroscopies. *Biotechnology and Bioengineering* **63**, 242-248 (1999).
52 Chung, T. M. *et al.* Helical phase driven by solvent evaporation in self-assembly of poly(4-vinylpyridine)-block -poly(l -lactide) chiral block copolymers. *Macromolecules* **45**, 9727-9733 (2012).
53 Shtukenberg, A. G., Punin, Y. O., Gunn, E. & Kahr, B. Spherulites. *Chemical Reviews* **112**, 1805-1838 (2012).
54 Gránásy, L., Pusztai, T., Tegze, G., Warren, J. A. & Douglas, J. F. Growth and form of spherulites. *Physical Review E - Statistical, Nonlinear, and Soft Matter Physics* **72** (2005).
55 Krebs, M. R. H., Bromley, E. H. C., Rogers, S. S. & Donald, A. M. The Mechanism of Amyloid Spherulite Formation by Bovine Insulin. *Biophysical Journal* **88**, 2013-2021 (2005).
56 Mansfield, E. H. On the buckling of an annular plate. *Quarterly Journal of Mechanics and Applied Mathematics* **13**, 16-23 (1960).
57 Oaki, Y. & Imai, H. Experimental demonstration for the morphological evolution of crystals grown in gel media. *Crystal Growth and Design* **3**, 711-716 (2003).
58 Elliott, J. C. *Structure and chemistry of the apatites and other calcium orthophosphates*. 1st edn, (Elsevier, 1994).
59 Pashley, D. H. *et al.* Collagen degradation by host-derived enzymes during aging. *Journal of Dental Research* **83**, 216-221 (2004).
60 Parkinson, C. R., Butler, A. & Willson, R. J. Development of an acid challenge-based in vitro dentin disc occlusion model. *Journal of Clinical Dentistry* **21**, 31-36 (2010).
61 Torres-Gallegos, I. *et al.* Enamel roughness and depth profile after phosphoric acid etching of healthy and fluorotic enamel. *Australian Dental Journal* **57**, 151-156 (2012).

62 Chen, H. *et al.* Synthesis of Fluorapatite Nanorods and Nanowires by Direct Precipitation from Solution. *Cryst Growth Des* **6**, 1504-1508 (2006).
63 Bertazzo, S. *et al.* Nano-analytical electron microscopy reveals fundamental insights into human cardiovascular tissue calcification. *Nature Materials* **12**, 576-583 (2013).
64 Bushby, A. J. *et al.* Imaging three-dimensional tissue architectures by focused ion beam scanning electron microscopy. *Nature Protocols* **6**, 845-858 (2011).
65 Larson, A. C. & Von Dreele, R. B. General Structure Analysis System (GSAS), Los Alamos National Laboratory Report LAUR. 86-748 (2004).
66 Harris, A. R. & Charras, G. T. Experimental validation of atomic force microscopy-based cell elasticity measurements. *Nanotechnology* **22** (2011).
67 Mohammed, N. R., Lynch, R. J. M. & Anderson, P. Inhibitory Effects of Zinc Ions on Enamel Demineralisation Kinetics in vitro. *Caries Research* **49**, 600-605 (2015).
68 Greenwald, S. E., Moore Jr, J. E., Rachev, A., Kane, T. P. C. & Meister, J. J. Experimental investigation of the distribution of residual strains in the artery wall. *Journal of Biomechanical Engineering* **119**, 438-444 (1997).
69 Tanaka, T. & Fillmore, D. J. Kinetics of swelling of gels. *The Journal of Chemical Physics* **70**, 1214-1218 (1979).

Figure legends

Figure 1| ELR spherulites & hierarchical mineralized structures. a) Photograph of a transparent, robust, and flexible statherin-ELR membrane before mineralization. The membrane's cross-section prior to mineralization b) imaged by SEM and c) histologically stained displaying a positive staining for both β-amyloid fibres (top) and elastin fibres (bottom) with Congo Red and Elastin von Gieson stains respectively. d) SEM image of the membrane's cross-section comprising of ELR nanofibers. e) Polarized light microscope (PLM) images depicting the presence of ELR spherulites with the characteristic birefringent Maltese-cross pattern on the surface and within the bulk of the membranes. f-i) SEM images of the top of an RGDS-ELR membrane after mineralization showing the hierarchical organization of the mineralized structures including f) aligned fluorapatite nanocrystals that are g, h) grouped into prism-like microstructures that further grow into i) macroscopic circular structures. j, k) The hierarchical structures grow until they meet each other, and l) can mineralize completely thin membranes. m) Rietveld refinement of an XRD pattern of mineralized membranes showing the fluorapatite nature of the crystalline phase with the

typical Bragg peaks of apatite. n) ^{19}F solid-sate MAS-NMR spectra confirming the presence of fluorapatite and CaF_2 (fluorite) phase at -103 and -108 ppm, respectively, with increasing fluorapatite peak intensity on the mineralized membrane (green) compared to without the ELP membrane (red) at the same conditions. o) Young's modulus and hardness relationship between the mineralized structures and different mineralized tissues. Scale bars: 5 mm (a), 20 µm (b), 40 µm (c-d), 200 nm (e), 10 µm (f), 3 µm (g), 200 nm (h), 1 µm (i), 10 µm (j), 20 µm (k), 30 µm (l), 20 µm (inset l), 5 µm (m), and 20 µm (n).

Figure 2| Bulk characterization. Organic-inorganic interactions within the bulk of the mineralized membranes. SEM observations revealed a) the abundant presence of a dense pattern of spherulite-like structures with b) a granulated central region at the bulk of the membranes' cross-sections, which c) template the growth of fluorapatite spherulites. d) Near the membrane surface, mineralized structures with nanocrystals grow vertically towards the surface of the membrane. DDC-SEM images of e) the core of fluorapatite spherulite structures located closer to the surface of the membrane and f) deeper within the bulk of the membrane, revealing a thin low-density material (green) surrounding a denser (orange) one. g) Back-scattered electron (BSE) image showing brighter areas at the centre of the structures, indicating the presence of mineral deep within the membrane. h) FIB sectioning of the hierarchically mineralized structure resolving the deeper mineralized core structures located underneath the centre of the structures. i) TEM images from a FIB milling liftout of the mineralized structures illustrating the change in growth direction of the nanocrystals from parallel to the surface towards the bulk of the ELR membrane, and j) the growing interface between the flat-ended inorganic crystals and the organic ELR material. k) HRTEM image of a single fluorapatite crystal showing its growth orientation and crystal lattices. l) SAED and FFT analyses showing the characteristic diffraction pattern of the fluorapatite crystals (left)

816 and its 10º co-alignment, respectively. Scale bars: 2 µm (a), 1 µm (b-c), 2 µm (d), 200 nm (e-
817 f), 20 µm (g), 5 µm (h-i), 200 nm (j), 100 nm (k), 10 nm (l), and 3 nm^{-1} (m).
818
819 **Figure 3| Protein disorder-order optimization and process tuneability.** a,b) Graphs
820 showing the different levels of ELR order and disorder as a function of cross-linking. The
821 levels of ELR ordered β-sheet structure and disordered random coil can be modulated and
822 tuned, while maintaining β-turn and α-helix conformations nearly constant. c) Table
823 summarizing the tuneability of the process including during both ELR matrix assembly
824 (Stage I) and the CaP nucleation and growth (Stage II). Scale bars: 3 µm (ELR spherulite
825 morphology), 20 µm (Apatite hierarchical structures), and 200 nm (Nanocrystal density).
826
827 **Figure 4| Mechanism of formation.** A schematic illustrating the two stages of the proposed
828 mechanism divided in I) ELR matrix assembly and II) calcium phosphate (CaP) nucleation
829 and growth.
830
831 **Figure 5| Resemblance between enamel and the hierarchical structures.** SEM images
832 illustrating the close resemblance of human dental enamel (a) to the hierarchically-ordered
833 mineralized structures (b) grown on a RGDS-ELR membrane at multiple length-scales. Scale
834 bars: 200 nm (a-b), 1 µm (c-d), and 20 µm (e-f).
835
836 **Figure 6| Dental applications of the hierarchical structures.** a) Application of the *in-situ*
837 cross-linked ELR membrane conformed over the rough and uneven surface of exposed
838 human dentin, exhibiting the hierarchical mineralized structures as a coating on top of the
839 native tissue. b, c) SEM images depicting b) a removed mineralized membrane with c) the
840 nanocrystals infiltrating, binding, and occluding the open dentinal tubule structures. d) FIB

841 milling of the mineralized coating at different depths to observe the dentin-membrane
842 interface, which exhibits infiltration of nanocrystals occluding the dentinal tubules. e) SEM
843 images revealing the effect of the acid attack at different time-points (15 minutes, and 7 days)
844 on both human dental enamel and the hierarchical mineralized structures. f) Graph illustrating
845 the Young's modulus and hardness of the human enamel and mineralized structures after the
846 acid attack. g) DDC-SEM images of the hierarchical mineralized structures after the
847 enzymatic digestion, showing a partially remaining organic material (arrow). Scale bars: 50
848 µm (a-b), 3 µm (c), and 10 µm (d), 1 µm (e), 500 nm (g). Error bars are represented as
849 standard deviation (SD) n = 10

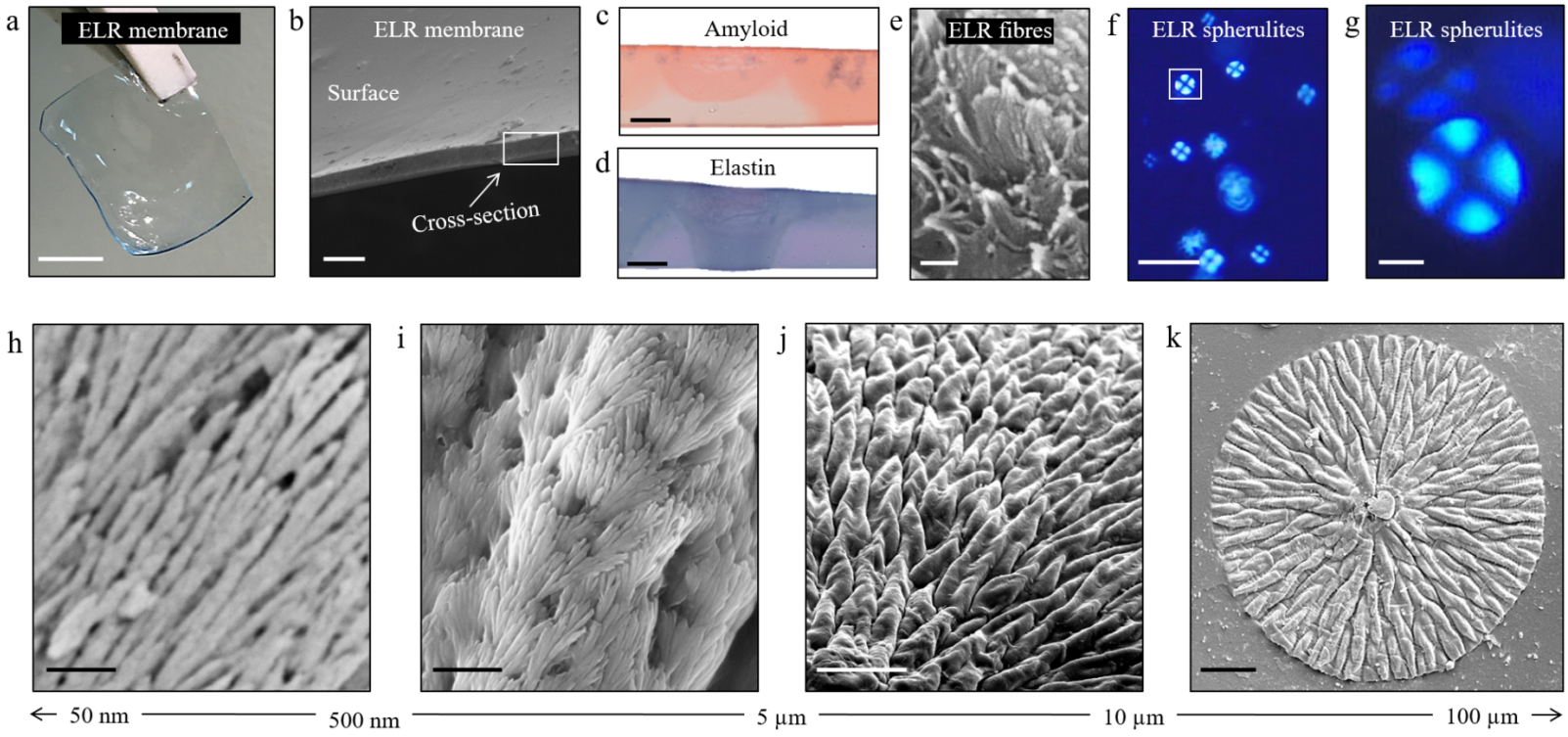
a
ELR membrane
b
ELR membrane
Surface
Cross-section
c
Amyloid
d
Elastin
e
ELR fibres
f
ELR spherulites
g
ELR spherulites
h
i
j
k
50 nm
500 nm
5 µm
10 µm
100 µm
l
m
n
o
XRD
121
030
002
Calculated data (C)
Observed data (O)
Fluorapatite phase
CaF2 phase
Difference (=O-C)
Arbitrary units (a.u.)
10
20
30
40
50
60
70
2 theta
p
MAS-NMR
CaF2
FAp
Without ELR membrane
FAp
CaF2
With ELR membrane
Arbitrary units (a.u.)
-80
-100
-120
-140
19F chemical shift (ppm)
q
Enamel
Hierarchical structures
Bone
Dentine
Young's modulus in GPa
80
60
40
20
0
0
1
2
3
4
Hardness in GPa

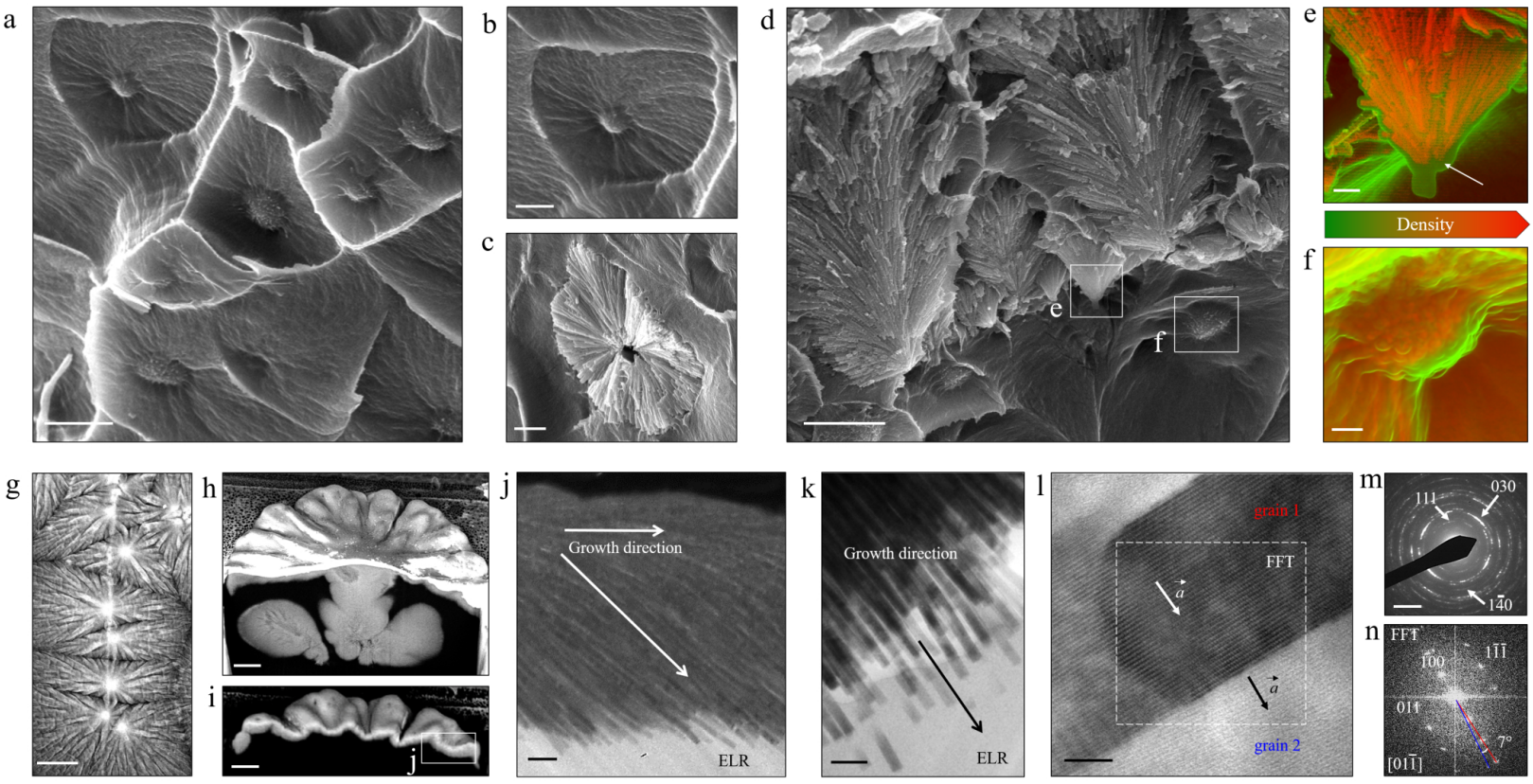
a
b
c
d
e
f
Density
g
h
i
j
Growth direction
ELR
k
Growth direction
ELR
l
grain 1
FFT
grain 2
m
111
030
140
n
FFT
100
011
7°

a

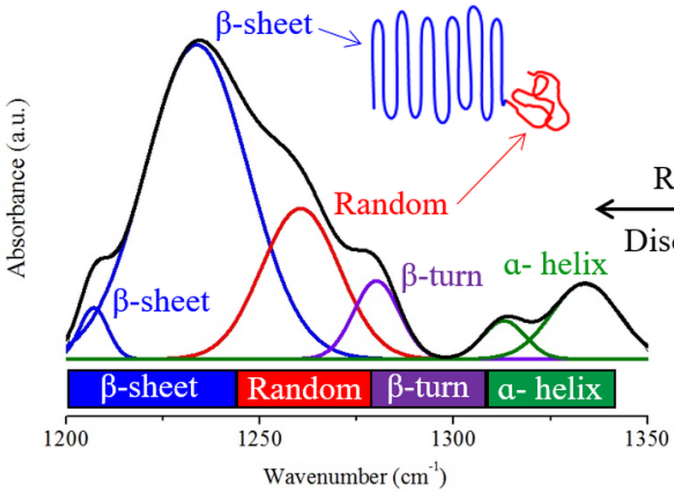

Random : β

Disorder : order

b

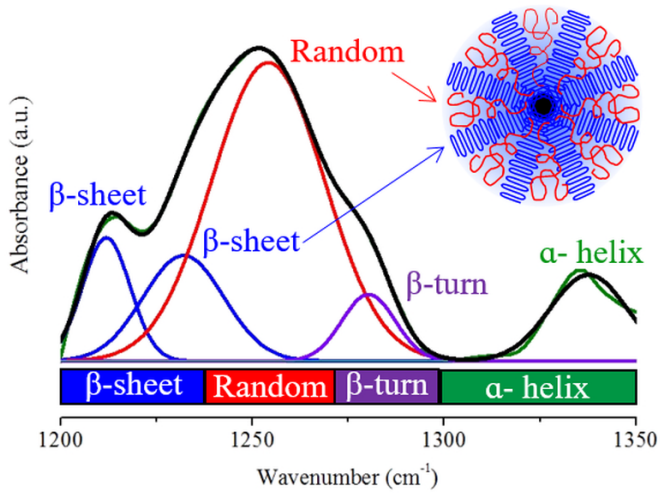

c

	ELR Crosslinks	0.25	0.5-1	3-6	12
I) ELR matrix assembly	Random : β ratio (Disorder : order)	0.26 ± 0.06	0.44 ± 0.02	0.87 ± 0.03	1.05 ± 0.17
	ELR spherulite morphology		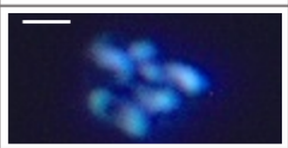	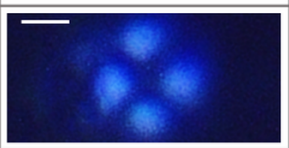	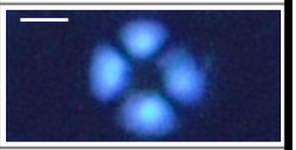
	# of ELR spherulites	x	0.17 sp/mm^2	3.24 sp/mm^2	5.38 sp/mm^2
	ELR stiffness	4.5 ± 0.8 kPa	48.3 ± 8.3 kPa	13.7 ± 5.7 MPa	11.4 ± 3.6 MPa
II) CaP nucleation and growth	Apatite hierarchical structures	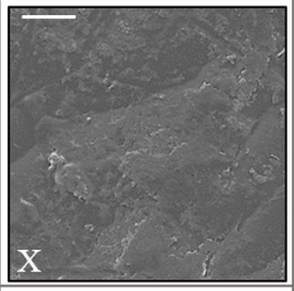 X	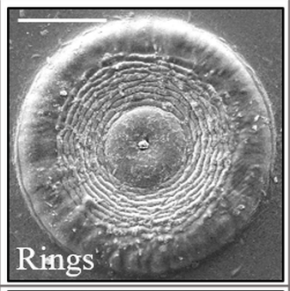 Rings	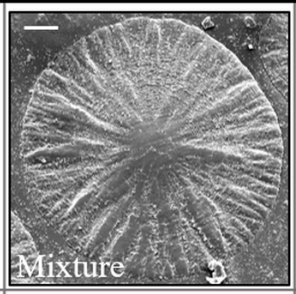 Mixture	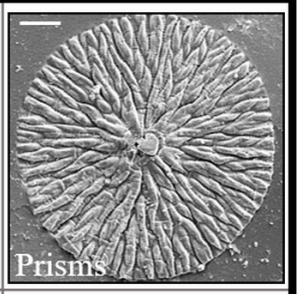 Prisms
	Nanocrystal density	x	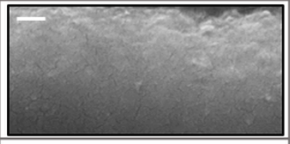	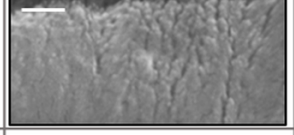	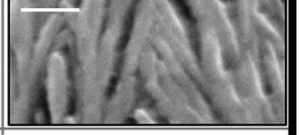
	# of structures	x	25.1 str/mm^2	55.8 str/mm^2	87.5 str/mm^2
	Stiffness	x	33 ± 20.1 GPa	17.7 ± 11.3 GPa	8.2 ± 1.4 GPa
	Hardness	x	1.08 ± 0.81 GPa	0.75 ± 0.25 GPa	0.57 ± 0.12 GPa

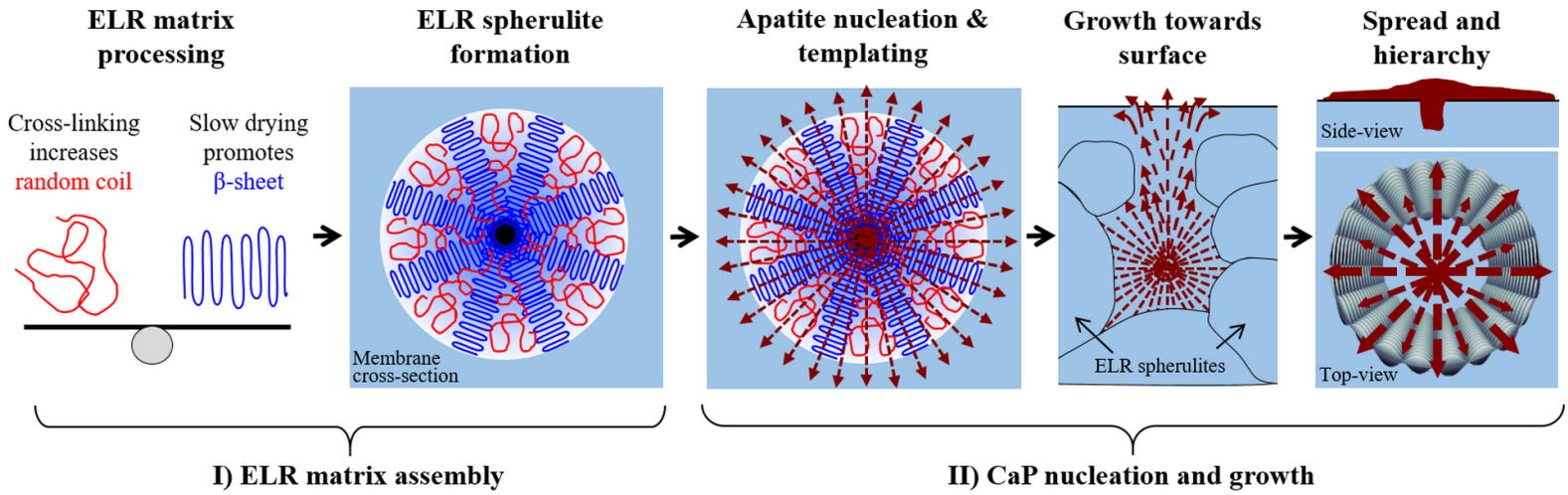
ELR matrix processing
ELR spherulite formation
Apatite nucleation & templating
Growth towards surface
Spread and hierarchy
Cross-linking increases random coil
Slow drying promotes β-sheet
Membrane cross-section
ELR spherulites
Side-view
Top-view
I) ELR matrix assembly
II) CaP nucleation and growth

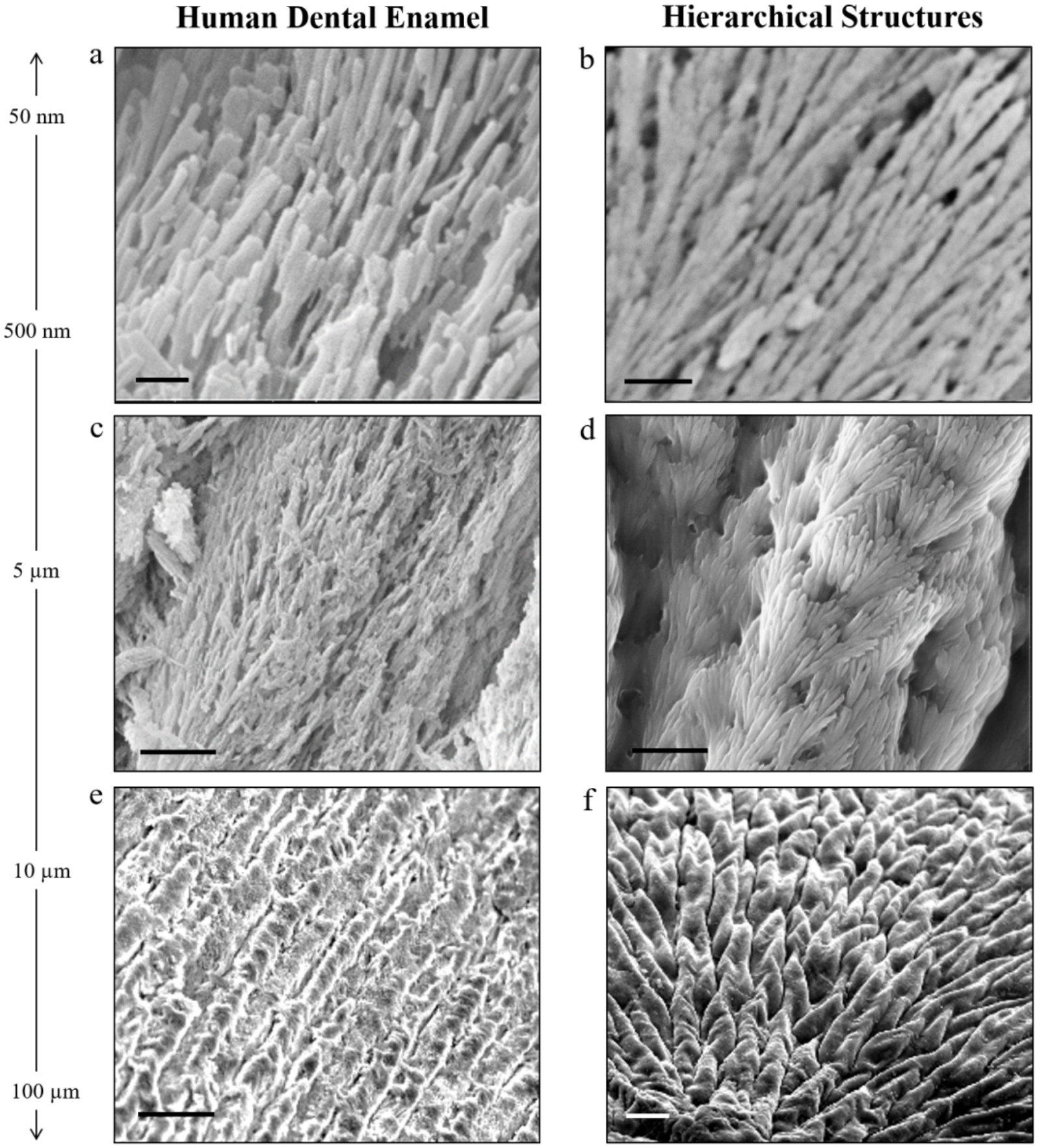
Human Dental Enamel
Hierarchical Structures
a
b
c
d
e
f
50 nm
500 nm
5 µm
10 µm
100 µm

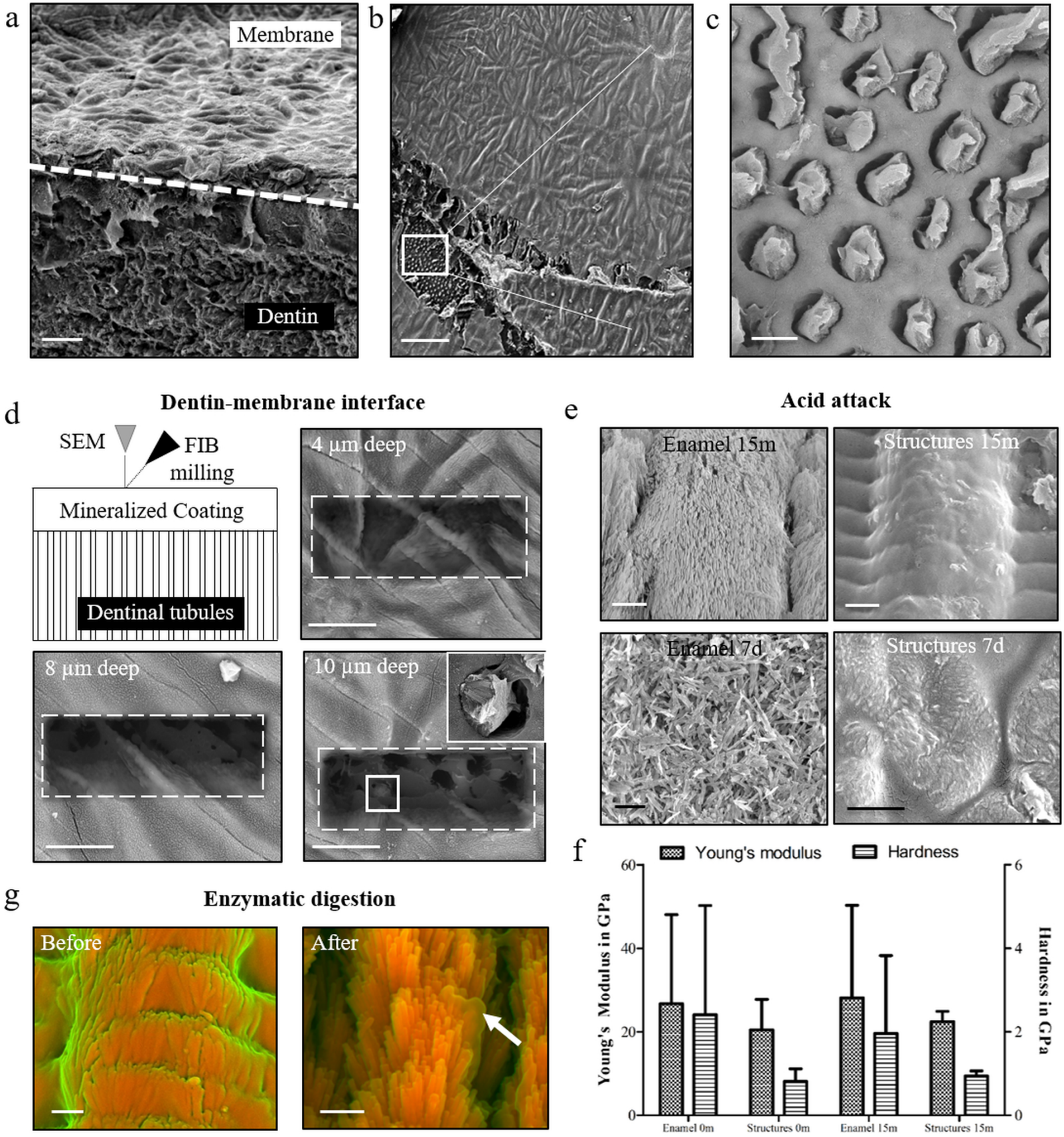
a
Membrane
Dentin
b
c
d
Dentin-membrane interface
SEM
FIB
milling
Mineralized Coating
Dentinal tubules
4 µm deep
8 µm deep
10 µm deep
e
Acid attack
Enamel 15m
Structures 15m
Enamel 7d
Structures 7d
f
Young's modulus
Hardness
Young's Modulus in GPa
Hardness in GPa
60
40
20
0
6
4
2
0
Enamel 0m
Structures 0m
Enamel 15m
Structures 15m
g
Enzymatic digestion
Before
After